International Journal of Minerals, Metallurgy and Materials
Accepted manuscript, https://doi.org/10.1007/s12613-020-2007-2
© University of Science and Technology Beijing and Springer-Verlag GmbH Germany, part of Springer Nature 2020

Curing time effect on mesocosmic parameters of cemented paste backfill through particle flow code technique

Lang Liu[1,2 *], *Jie Xin*[1], *Chao Huan*[1], *Yujiao Zhao*[1], *Xiang Fan*[3], *Lijie Guo* [4], *and KI-IL Song*[5]

1) Energy School, Xi'an University of Science and Technology, Xi'an 710054, China
2) Key Laboratory of Western Mines and Hazards Prevention, Ministry of Education of China, Xi'an 710054, China
3) School of Highway, Chang'an University, Xi'an 710064, China
4) Beijing General Research Institute of Mining & Metallurgy, Beijing 100160, China
5) Dept. of Civil Engineering, Inha University, Incheon 402-751, South Korea

Corresponding author:

*Lang Liu: liulang@xust.edu.cn

Email addresses for co-authors:

Jie Xin (17203078017@stu.xust.edu.cn), Chao Huan (huanchao@xust.edu.cn)

Yujiao Zhao (zhaoyujiao@xust.edu.cn), Xiang Fan (fanxiang224@126.com)

Lijie Guo (guolijie@bgrimm.com), KI-IL Song (ksong@inha.ac.kr)

Accepted Manuscript Not Copyedited

Abstract: Several special mechanical properties such as the dilatancy and compressibility of cemented paste backfilll (CPB) are controlled by the internal microstructure and its evolution. To explore the mesocosmic structure changes of CPB during the development process. Based on the scanning electron microscopy (SEM) and mechanical test results of CPB, the particle size information of CPB was extracted, and a two-dimensional (2D) particle flow code (PFC) model of CPB was established to study the evolution rule of mesoscopic parameters during CPB development. The FISH language of the PFC was used to develop a program for establishing a PFC model according to SEM results. The mesoscopic parameters of CPB samples at different curing times, such as the coordination number (C_n), contact force chain, and rose diagram were obtained by recording and loading; these were used to analyze the intrinsic relationship between mesoscopic parameter variations and macroscopic mechanical response during CPB development. It is of great significance to establish the physical model of CPB by using PFC to reveal the mesoscopic structure of CPB.

Keywords: Cemented paste backfill, particle flow code method, scanning electron microscopy, mesoscopic parameter, fabric

Accepted Manuscript Not Copyedited

1 Introduction

Large amounts of tailings produced by the mining industry pose a serious threat to the environment [1-6]. Because its annual emissions are close to 10 billion tons in China, Tailings is one of the most important recycling materials in the mining industry [7, 8]. The efficient treatment of tailings is a common concern in the industry. CPB is an alternative way of using tailings for underground backfilling [9, 10], which can effectively reduce labor and material costs, prevent land subsidence and improve ground support and working environment [11, 12]. For detailed explanation of the CPB technology, interested readers can refer to the review paper of Ref [13]. All these advantages and potential functions lead to the wide application of CPB in the world. [14-19].

CPB is an engineered, non-segregating, flowable, high-density and homogenous backfill material consisting usually of tailings, cement, mix water and sometimes additive (chemical or mineral) [20-22]. Mechanical properties (such as stress transmission, failure mode, and bearing capacity) of these various components are vastly different under the action of self-weight pressure. Consequently, the properties of CPB and rock masses exhibit a large difference. The quality and performance of CPB rely significantly on the internal structure and external influencing factors, such as hydration products content, surface properties of aggregates and the grading of tailings [23, 24].

Owing to the complexity of the model, most current discrete element simulations of meso-mechanical properties involve the random simulation of regular blocks. The model in this paper is based on the particle splicing of SEM images of CPB, which can restore the real internal structure of CPB. The established model can simulate the mechanical behavior of CPB more accurately and can be applied to other engineering materials, such as concrete, soil and so on.

Generally, granular materials (concrete, soil, CPB, etc.) exhibit properties (homogeneity, workability, durability, etc.) in macrostructure, while they show diversity

Accepted Manuscript Not Copyedited

and volatility in mesostructure, which are closely related. The mechanical properties of granular materials are controlled by the microstructure / mesostructure and its evolution. The failure and deformation of granular materials are often related to changes in mesostructure characteristics, which had been studied extensively in the literature [10, 25-29]. For example, Kong et al. extracted microscopic information that was difficult to obtain in a laboratory test. The microscopic mechanism of sandy soil was discussed by analyzing the macroscopic mechanical properties, displacement field, strain field, particle orientation, velocity field, C_n, and contact force chain [26]. Xu et al. used PFC to simulate the crack propagation and crack propagation pattern of CPB samples at different notch locations, and found that PFC was an effective numerical analysis method to explore the fracture mechanism of CPB microcrack [10]. Liu et al used PFC2D to analyze the structural changes of CPB under uniaxial compression load, and studied the influence of internal sulfate attack (ISA) on the failure mode of CPB, and researched the failure mode of CPB by adopting the displacement vector of CPB, it was found that CPB particles were mainly subjected to tensile stress during the failure process [27]. Song et al. implemented the acoustic emission (AE) three-dimensional monitoring system into PFC and established a three-dimensional multilayer stress corrosion model (MSC) for concrete under multi-stage cyclic compression load [28]. However, the study above mainly used the PFC model to quantitatively characterize the macroscopic mechanical properties and mesoscopic parameters in a failure process. Moreover, most of the particles used in the PFC model were generated randomly according to a certain gradation and cannot accurately simulate the mesoscopic parameters and mechanical properties of materials. The relationship between mesoscopic parameters and macroscopic mechanical properties has not been studied thoroughly.

Although a numerical simulation cannot completely replace an experiment to simulate the development of CPB, it can be used as an alternative to simulate the mesostructure

Accepted Manuscript Not Copyedited

problem of particle development. Based on the SEM image of CPB, the particle size information of CPB was extracted, and the PFC model of CPB was established to restore the real internal structure of CPB. Then, the servo function in the established PFC model is used to match the stress-strain curve of CPB under uniaxial compression. The mesoscopic parameters of CPB samples at different curing times, such as the C_n, contact force chain, and rose diagram were obtained by recording and loading; these were used to analyze the intrinsic relationship between mesoscopic parameter variations and macroscopic mechanical response during CPB development.

2 Materials and methods

2.1 Material

2.1.1 Material usage

In this study, 32 cylindrical CPB specimens (D*H = 50*100 mm) were prepared. The elastic modulus and deformation characteristics of uniaxial compressive strength (UCS) were tested on 12 specimens. 12 CPB specimens were scanned by electron microscopy to determine the internal particle and pore structure of CPB during development. The remaining 8 samples were used as spare samples; the specific experimental arrangement of the CPB is shown in Fig. 1. CPB specimens were prepared with different curing periods (3, 7, 14, and 28d), and the height and diameter of each specimen were measured with a vernier caliper before the UCS tests. Then, four different curing periods of CPB were tested accordingly. For the CPB sample in each curing time, three samples were used for UCS test and another three samples for electron microscopy, while the remaining CPBs were treated as spares.

2.1.2 Material characterization

The backfill test materials were as follows: full tailings of tungsten mine, Portland composite cement with strength grade 425 (P.O 42.5), and urban tap water. Among them, the nature of tailings was especially important in CPB. The tailings used came from a

Accepted Manuscript Not Copyedited

Xianglushan Tungsten Mine in Jiangxi province, China. Fig. 2 shows the particle size distribution determined by a laser diffraction particle size analyzer (Malvern Mastersizer, 2000) [30]. As shown, the grain sizes at d_{10}, d_{50}, d_{90} and C_u were 11.8 μm, 80.3μm, 216.6μm and 8.55, respectively. It was determined that the content of fine particles (20 μm) of the tailings was 15.95%, and the tailings could be classified as coarse tailings material [16]. The basic physical properties of tailings were determined, as shown in Table 1. The specific surface area and specific gravity of the tested tailings samples were 212.4 cm^2 /g and 2.992 respectively. The primary chemical composition (as shown in Fig. 3) was obtained with an X-ray diffraction (D/Max-3B, Japan). Portland cement (P·O 42.5) was selected as the binder for CPB, and the main physical properties are shown in Table 2. Table 3 shows the chemical composition of P·O42.5 determined by an X-ray fluorescence spectrometer (S8 Tiger). Considering the requirement of slurry fluidity of CPB, the designed solid slurry concentration is 72% to ensure that the slump is within the range of 170mm - 250mm, which can be successfully transported to the underground [14]. According to the engineering application of Xianglushan tungsten mine and the recommendation of literature [2], the tailings / cement ratio is 6. Therefore, the experiment design of CPB is shown in Table 4.

2.2 Experimental procedure

Firstly, the basic physical properties and chemical composition of tailings were determined. Secondly, the tailings, cement and water were thoroughly stirred to prepare cemented CPB slurry, which was then poured into a standard cylindrical mold. Thirdly, after the filling was completed, the specimens were placed for 24 hours. After the specimens were formed and demoulded, the CPB was put into the constant temperature and humidity curing box (temperature (20 ± 1) °C, humidity (95 ± 1%)) [31]. Fourthly, UCS and micro-test were carried out when CPB reached the corresponding curing time. Finally, the PFC model of the CPB was established according to the SEM obtained by the microscopic experiment, then

Accepted Manuscript Not Copyedited

the mesostructure of the backfill was analyzed.

2.3 SEM processing and acquisition of CPB particles

Appropriate samples of CPB at different curing times were selected to render the desired size (diameter ×height =5mm ×5mm) of electron microscopy samples, and the samples were processed with gold spraying for 180s [32]. To obtain the mesoscopic characteristics of the developing CPB, SEM images with a magnification of 100X at different positions were scanned at the same curing time. In SEM, for an image with unclear positions, the focal length of the image must be adjusted repeatedly until the image was clear. As shown in Fig. 4, all the SEM images (280 samples from three sets of CPB) were obtained from the same magnification at different curing times (3, 7, 14 and 28 d).

Table 1 Physical properties of tailings used in this study

Item	Specific gravity	Volume-weight (t/m^3)	Porosity (vol. %)	Natural repose angle (°)	Specific surface area(cm^2/ g)
Tailings	2.992	1.674	34.659	42.997	212.4

Table 2 Main physical properties of P·O42.5 Portland cement

Item	Value	Reference value
Fineness (<0.045 mm) (%)	11	≤30
Initial setting time (min)	162	≥45
Final setting time(min)	203	≤390
Tensile strength after 28d [19]	6.6	6.5
Compressive strength after 28d [19]	41.5	42.5

Note: reference of P·O42.5 Portland cement was from China’s cement strength classification [33].

Accepted Manuscript Not Copyedited

Table 3 Chemical composition of P·O42.5 Portland cement

Composition	CaO	SiO_2	Al_2O_3	Fe_2O_3	MgO	SO_3	K_2O	Na_2O	TiO_2	Others
Content (%)	64.13	19.19	4.50	3.33	1.82	1.06	1.04	0.41	0.24	2.28

Table 4 Experimental design

Item	Slurry concentration (%)	binder	Tailings–cement ratio
Value	72	P·O42.5	6

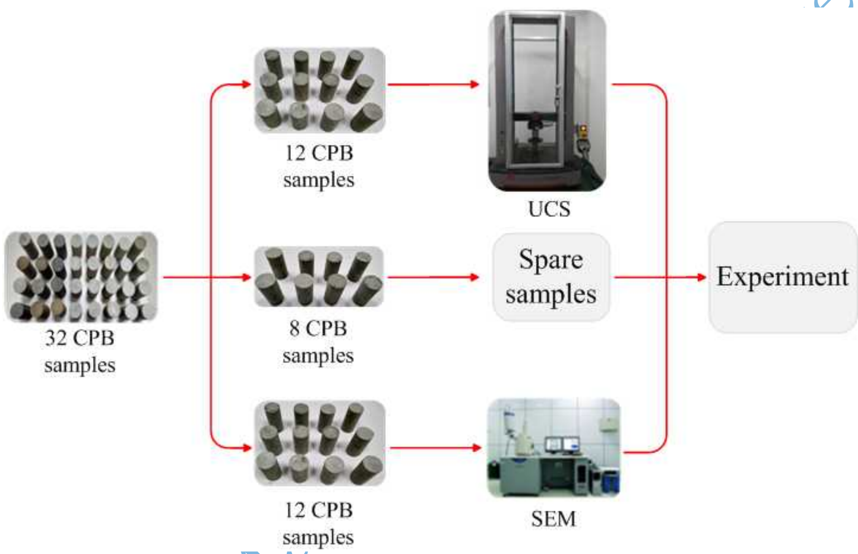

Fig.1 Experimental arrangement of CPB samples

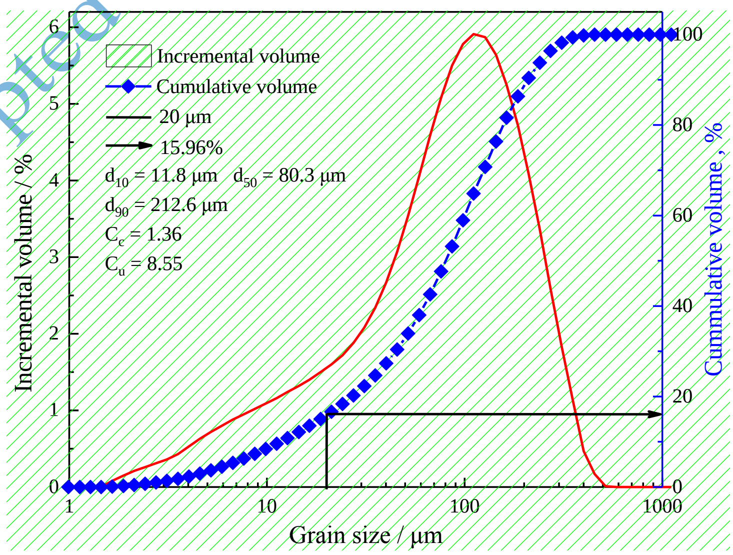

Fig.2 Tailings particle size distribution curve

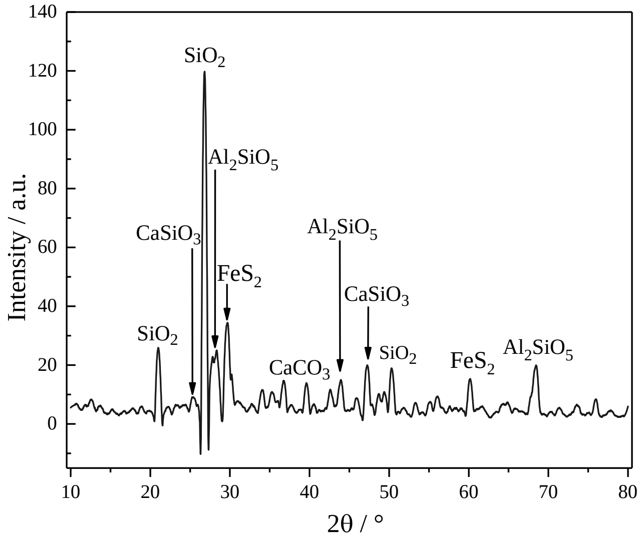

Fig. 3 Chemical characteristics of tailings obtained using X-ray diffraction

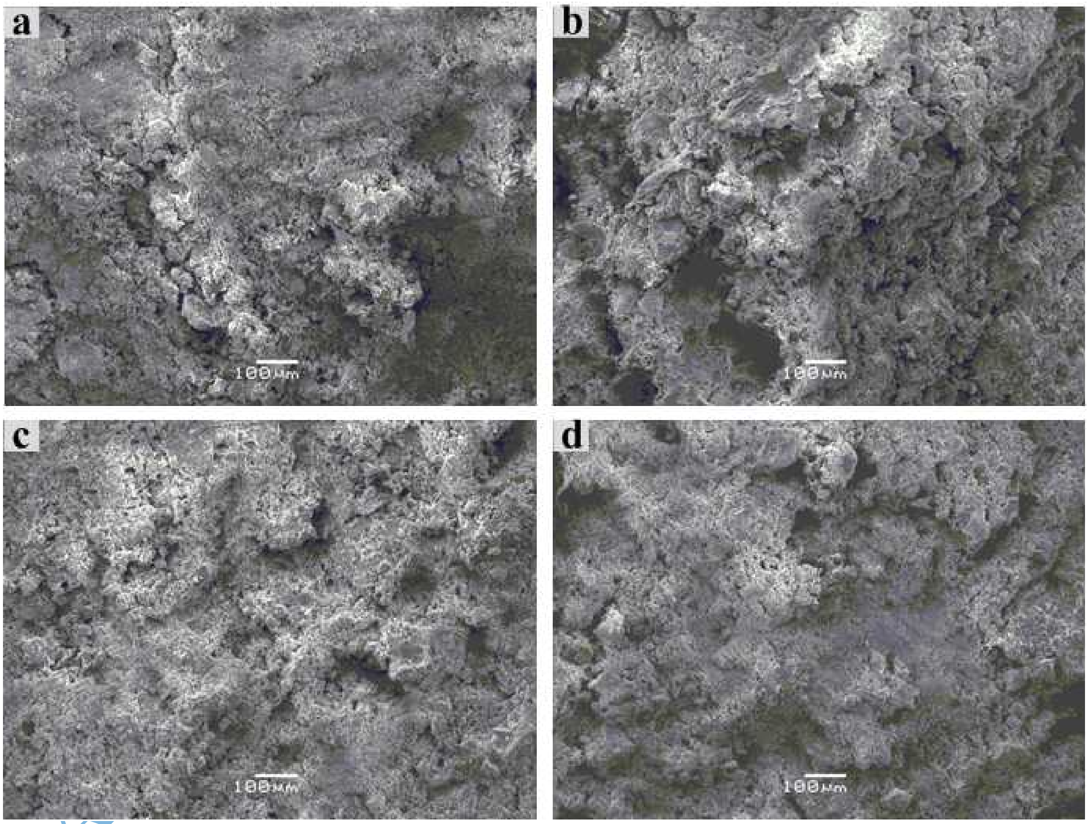

Fig. 4 SEM images of CPB at different curing times: (a) 3d (b) 7d (c) 14d (d) 28d

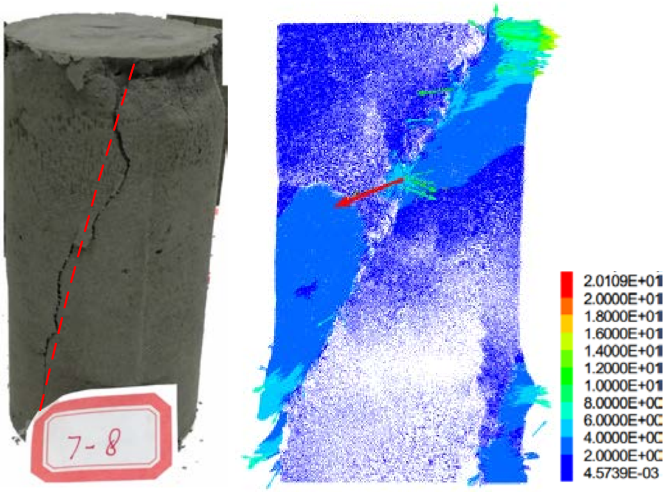

(a) (b)

Fig. 5 Failure mode of CPB: (a) experimental failure model and (b) velocity vector diagram during failure

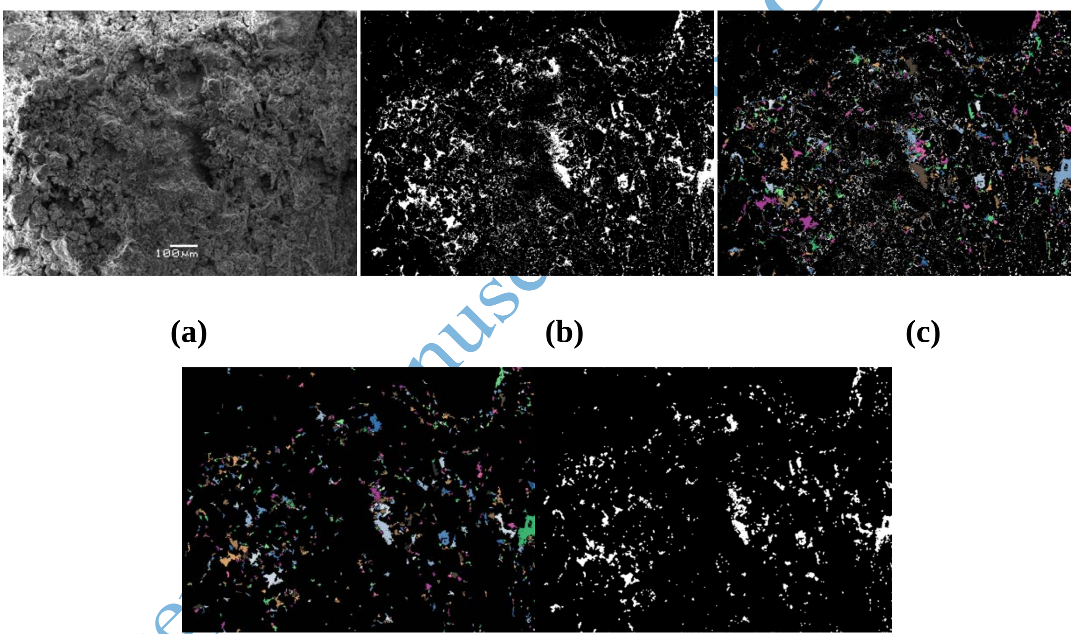

(a) **(b)** **(c)**

(d) **(e)**

Fig. 6 Illustrations of SEM image processing, identification, and acquisition (a-f represent the imaging results of noise removal, multiple threshold segmentation, pore bridge, noisy-particle elimination, and background extraction, respectively)

2.4 UCS test

Considering the economic cost of the test, the practicability of the test method, and the recommendations of the test and literature [34], MTS C43.504 press was selected. A computer-controlled 20-kN press was loaded at a constant speed of 1 mm / min until specimens failed according to ASTM1424-10 standard practice [35]. When the strength of the CPB samples reduced to 70% of the peak strength, the UCS tests were completed; the data were then compiled, the UCS were calculated, and the stress–strain curves were obtained. Fig.5 shows the experimental failure mode of CPB specimens and the velocity vector when simulating CPB failure [27]. As shown in Fig. 5(a) and Fig. 5(b), the velocity vector of numerical simulation of CPB failure corresponded to the experimental failure mode, which can reflect the failure mechanism of CPB. In the failure mode of CPB sample, the sample belonged to single incline plane shear failure, which was caused by the shear stress exceeding the limit on the failure surface.

2.5 Particle flow code modeling

The test CPB sample is concrete-like, and it is more accurate to set the parallel bonding according to the contact bond between particles used in this study and particles used in corresponding studies [36], which also eased the numerical simulation process. Using SEM images of CPB with different curing times as an example, the modeling steps were introduced [37]. According to the proposed modeling idea, the real mesostructure model can be established quickly in a 2D environment. The CPB development numerical test was performed. The specific steps are as follows:

(i) The original SEM image quality was insufficient and cannot meet the basic requirements of accurate image analysis. To improve the quality of the SEM images, the following special image processing methods were used to analyze the CPB particles [38]. Fig.6 illustrates the results of SEM image processing and acquisition, including noise removal, multiple threshold segmentation, pore bridge, noisy-point elimination, and pore extraction. Owing to various external adverse factors in the laboratory (such as SEM luminosity, and incompleteness of gold spraying in CPB), the SEM of CPB treated by the

Accepted Manuscript Not Copyedited

steps in Fig.6, which was used directly for the analysis of the corresponding internal structure of the section, which was not sufficiently representative. Therefore, because the physical model size of the actual CPB (length × height = 50 mm × 100mm), and the SEM scan image size (length × height = 3.75 mm × 5mm) of different parts of CPB pertain to the same curing time, it was necessary to stitch the SEM images together (14 horizontally, 20 vertical). The stitched model was slightly larger than the actual size. Such that the CPB particles were more random and representative, the model size of this curing time was cut out randomly from the assembled image.

(ii) Using the SEM image of step (i) and different CPB parts at different curing times, the development procedure of this study was established. The generated PFC2D model was executed. The total numbers of balls that were generated to the CPB particles were 83792, 84746, 88691, and 87012. As shown in Fig.7, the black part was the CPB particle, which was simulated with PFC balls, and the white part was pore.

(iii) According to the output of the data file exported by the program, the mechanical property boundary conditions of the corresponding materials were given by to the ID number of the ball. The physical model of the CPB established by PFC2D was used to match the stress-strain curve obtained in the UCS of the backfill [39]. Furthermore, the parameters of CPB were obtained as shown in Table 5. The geometric model after importing the PFC2D model was shown in Fig. 8. The SEM image was observed to be entirely consistent with the internal structure, and the modeling process was easily completed within 1 hour. The PFC2D model simulated the developmental test samples of the model above. The interaction between the CPB particles and the pore structure can be studied well from the perspective of the mesostructure, which was crucial for the further study of macroscopic mechanical behavior. The flow chart of the complete experiment is shown in Fig. 9.

Accepted Manuscript Not Copyedited

Table 5 Micro-properties for discrete element simulation

Property	CPB particles			
	3d	7d	14d	28d
Stiffness ratio, kn/ks	1	1.2	1.35	1.5
Modulus of elasticity, edom	5×10^{8}	2×10^{9}	2.5×10^{9}	1.5×10^{9}
Contact normal strength, pb_ten	1.5×10^{6}	2×10^{6}	2×10^{6}	2.8×10^{6}
Contact shear strength, pb_coh	5×10^{6}	1.5×10^{7}	3.5×10^{7}	6.5×10^{6}
Parallel bonding friction angle, pb_fa	0	0	0	0
Damping coefficient, ζ	0.5	0.5	0.5	0.5
Friction, *f*	0.3	0.5	0.75	0.9

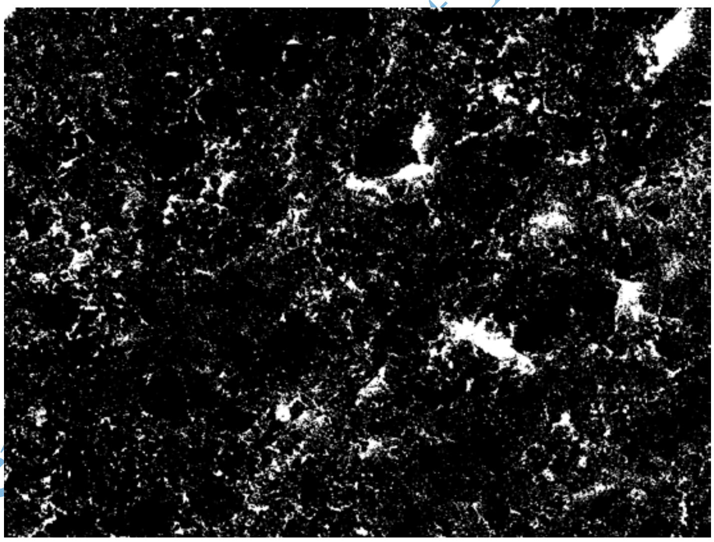

Fig. 7 Particles and pores of CPB

Acce… Not Copyedited

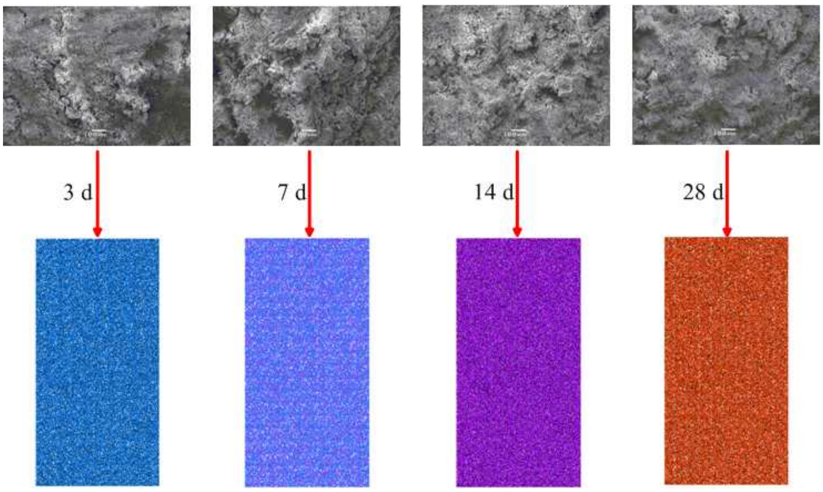

Fig.8 PFC model of CPB particles based on SEM

Fig.9 Experimental process

3 Results and discussion

3.1 Generation and verification of PFC model

The shape of the model was rectangular with length × height = 50 mm × 100 mm; the size was set as the real size of the CPB sample. Particle generation was based on the PFC model described in section 2.5. The CPB specimens at different curing times were subjected to numerical simulation. The contact model adopted a parallel contact and provided loading for the UCS test, as shown in Fig.10. Comparing the UCS and stress–strain curves of CPB samples at different curing times, the numerical simulation was matched with each stress–

Accepted Manuscript Not Copyedited

strain curve, the parameters were adjusted, and finally the numerical curves closest to the actual experimental results were obtained. As shown in Fig.11, as the strain increased, the stress of the CPB with the curing time of 28d was significantly higher than that of the CPB at other curing time. This indicated that with the increase of CPB curing time, the sufficient hydration of CPB results in the increase of CPB strength [40]. The loading rate is the basic parameter of dynamic mechanics research and the loading rate effect of mechanical properties of CPB can provide some references for the failure mechanism of backfill. During the failure of CPB under the action of constant loading rate, the pore structure rapidly developed and expanded until it was destroyed. In addition, the slope of the stress-strain curve of CPB was slower before the peak and steeper after the peak. It can be seen from the Fig.11 that the PFC model of CPB based on the SEM image can better simulate the stress-strain curve of the CPB sample, including the elastic modulus and the peak stress. The CPB particle mesoscopic parameters under each numerical model were obtained.

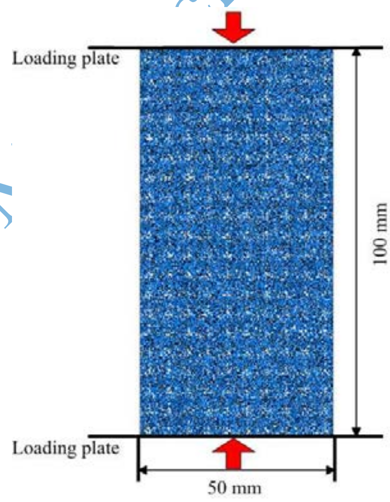

Fig.10 PFC test model (83792 ball)

Accepted Manuscript Not Copyedited

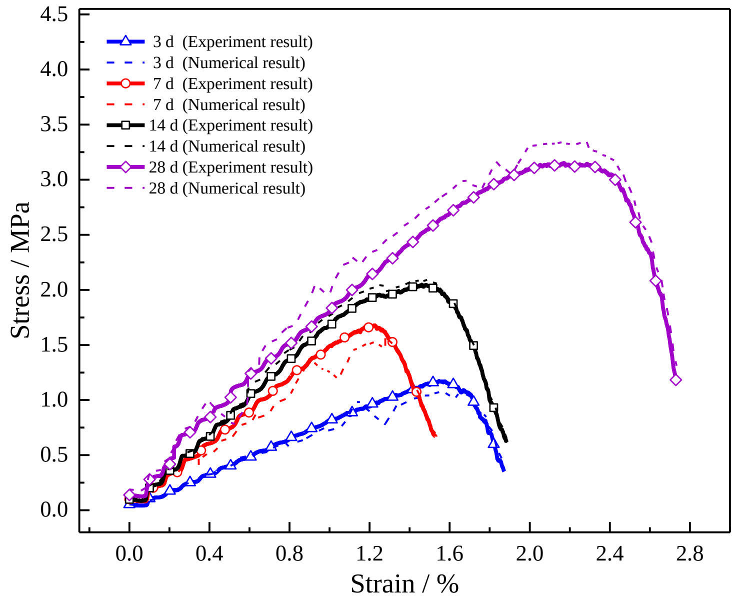

Fig. 11 Comparison of the stress–strain curves from the laboratory specimens and numerical models

3.2 CPB coordination number

The coordination number (C_n) is defined as the average number of contacts between a ball or a clump and the surrounding particles or clusters [41]. It is used to describe mesostructural features such as the particle contact density [42]. It can be expressed as follows:

$$c_n = \frac{\sum N_b n_c^{(b)}}{N_b} \tag{1}$$

Where N_b is the total number of particles or clusters of particles whose center ID is in the measuring circle, and $n_c^{(b)}$ is the number of contacts around block *b*. It is known that the C_n is based on the average concept.

The C_n was mainly related to factors such as initial void ratio, intergranular friction coefficient, particle gradation, and particle geometry. A measuring circle with a radius of 5 mm was set in the center of the CPB sample [26]. The variation in coordination with strain during CPB development was obtained, as shown in Fig. 12. Self-weight stress is the stress caused by self weight of CPB. The self weight stress within the backfill in the vertical

Accepted Manuscript Not Copyedited

direction is equal to the mass of the filling body column per unit area above this point. The essence of change in the mechanical properties of the CPB was the rearrangement of CPB particles under self-weight pressure. The sliding and rotating reorganization of such particles inevitably resulted in changes in the C_n. Fig. 12 shows the relationship between the C_n of CPB and strain. The results showed that with the increase of strain, the C_n of CPB with the curing time of 28d was higher than that of other CPBs of other curing times. The possible reason was that the longer the hydration curing time of CPB, the more frequent the CPB contacts of particles under the influence of self-weight pressure. Each point in the Fig.12 corresponded to the development morphology of CPB. Combined with Fig. 11, when the strain of CPB reached 0.45% - 0.6%, the C_n of CPB was in the approximate horizontal line, which corresponded to the stable development stage of micro-elastic cracks in CPB. When the strain reached 1.35% - 2.25%, the C_n of CPB was in a sharp decline, which corresponded to the failure state of CPB.

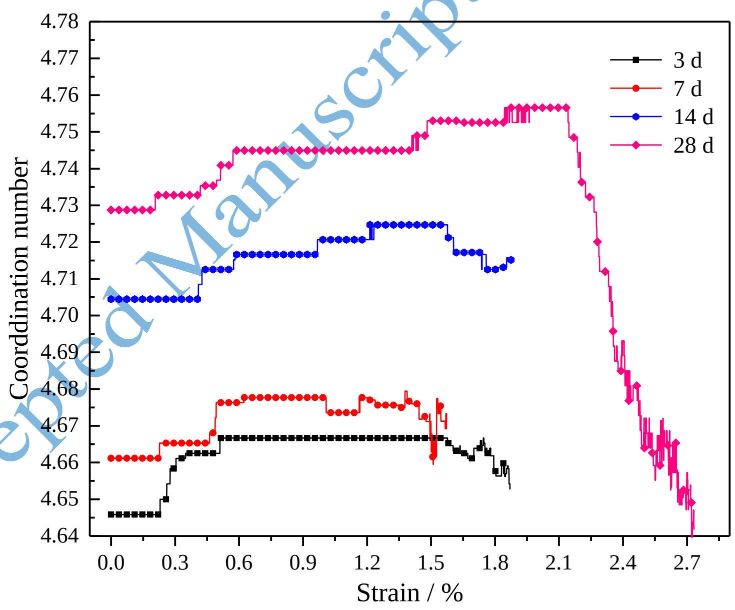

Fig. 12 Changes in C_n in the development of CPB

3.3 CPB porosity

Quantitative measurement technology of particle and pore identification and analysis system independently developed by Xi'an university of science and technology was

Accepted Manuscript Not Copyedited

adopted to conduct quantitative analysis of SEM images by using statistical and other related theories, and then the porosity of CPB was obtained [43]. Quantitative results of porosity was in agreement with the results of Sun et al [39] and Liu et al [34]. Especially，It was discussed in detail that the porosity content of sulphur-containing CPB ranged from 8% to 13% during 3d to 28d in curing time, and the content of this porosity was consistent with Liu et al [34] from studies in pore and strength characteristics of sulphide CPB. Furthermore, Due to the presence of coarse particles in tailings grading (Cu > 6), the gap of coarse particles are just occupied by fine particles, which leads to the full cementation of cement tailings and water, thus leading to the low porosity of CPB. Therefore, the initial porosity of PFC model was set by using the porosity of quantitative analysis. Fig. 13 shows the change in porosity versus strain for CPB of different curing times. The porosity remained substantially stable with a change in strain during the same curing time. When the curing time was 3d, its maximum porosity was approximately 16%. With the development of CPB, when the curing time was 28d, its maximum porosity was approximately 13.7%. The reason for the decrease in CPB porosity was that hydration products formed during CPB development, such as hydrated calcium silicate, ettringite, and calcium hydroxide, was enriched in macropores in the early development stage, and the particles were interdependent and intertwined [44]. Consequently, the particle spacing was reduced continuously, and some of the pores were gradually enriched, thus resulting in a decrease in the CPB porosity. The relationship between porosity and strain is shown in Fig. 13. Each point in the Fig.13 corresponded to the development morphology of CPB. When the strain of CPB reached 1.8% - 2.0%, the porosity of CPB decreased by about 1.09% and the stress reached 80% - 90% of the peak value in 28 d of curing time, combined with Fig. 11. When the strain increased to 2.2% and the porosity decreased by about 1.44%, the stress of CPB reached the stress peak, which corresponded to the failure critical point of CPB. In addition, the stress-strain and porosity of the CPB had similar rules in other curing time.

Accepted Manuscript Not Copyedited

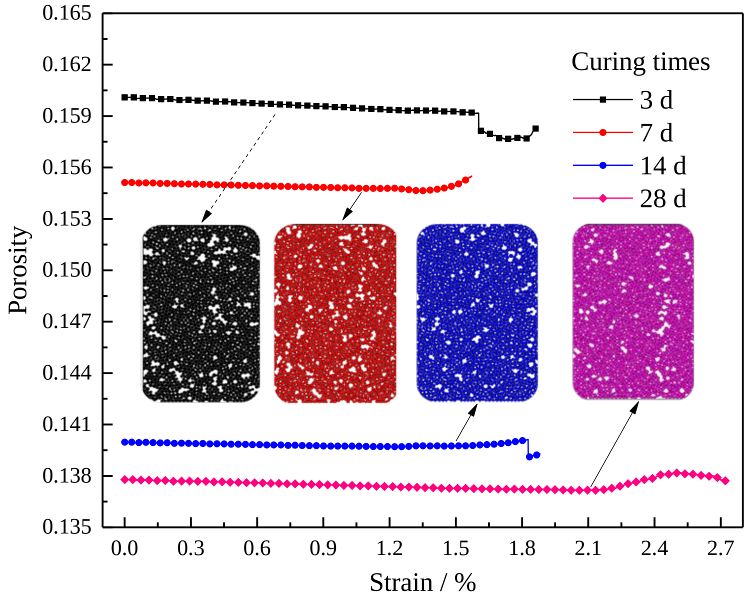

Fig. 13 Changes in porosity in the development of CPB

3.4 Velocity field of CPB

Fig. 14 shows the velocity field variation during the development of CPB. At the curing time of 3d and 7d, the CPB particles tended to move in all directions. The edge particles exhibited a higher velocity, and the intermediate particles moved at a lower speed. This was because the edge particles were more likely to move under the effect of the self-weight pressure. As CPB development progressed, the moving speed of the intermediate particles decreased slowly, the velocity of the particles at the edge tended to decrease, and all the particles tended to be disordered. At 28d, the velocity of CPB particles decreased and tended to be stable, but the pore direction was more disorderly. The overall variation was similar to the results of laboratory tests but more intuitive and clearer.

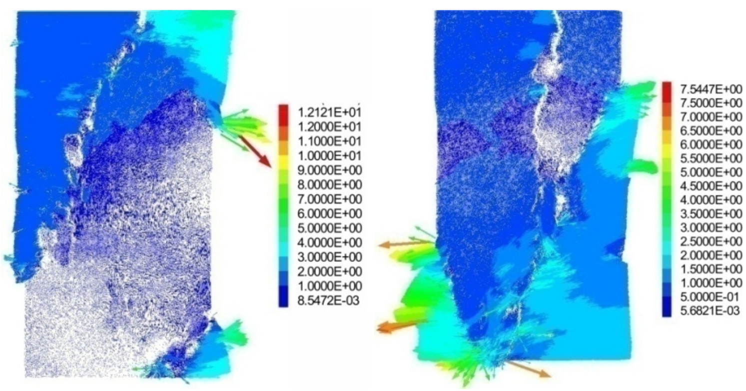

(a) (b)

Accepted Manuscript Not Copyedited

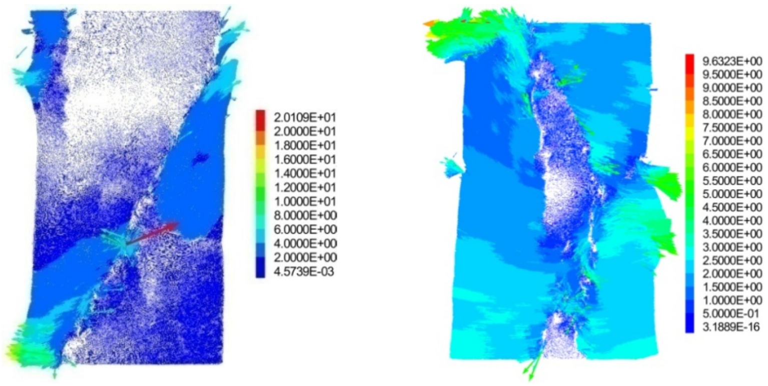

(c) (d)

Fig. 14 Evolution of velocity field in the development of CPB at different curing times: (a) 3d (b) 7d (c) 14d (d) 28d

3.5 Rose diagram of CPB

The CPB sample consists of discrete particles of different shapes and sizes arranged randomly by interaction that exhibited significant anisotropic characteristics. “Fabric” is a commonly used index reflecting the anisotropy of materials [45]. It referred to the distribution of the direction of particles in indirect contact [46]. Fig. 15 shows the evolution of the normal contact rose diagram during the development of CPB. When the curing time was 3-7d, the overall contact of the sample in all directions was relatively uniform. When the curing time was 14-28d, the CPB was affected by the self-weight pressure. The contact direction mainly concentrated on 80–100° and 260–280°, demonstrating obvious anisotropy. This was because in the development of CPB, rotation was the main movement state, and translation was the supplement, which easily caused the change in contact state between particles. Meanwhile, owing to the constraint of friction between particles, the contact direction changed, and the fabric distribution was various.

Accepted Manuscript Not Copyedited

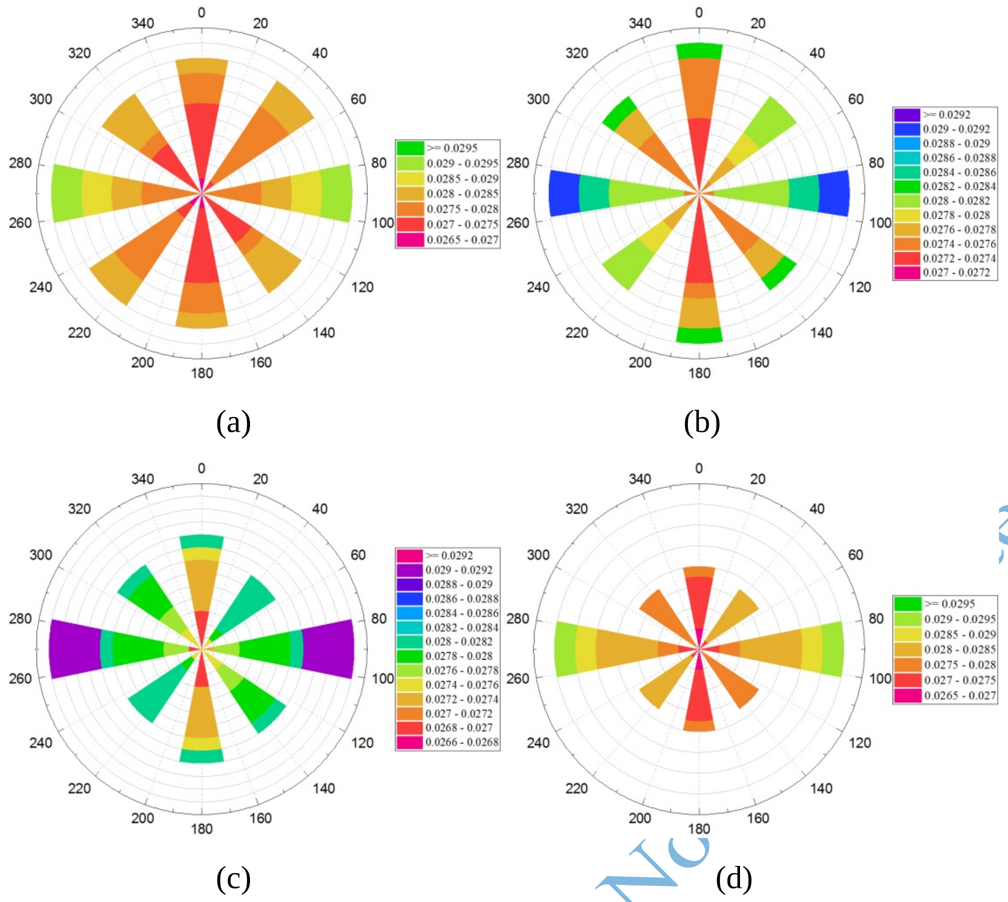

Fig. 15 Evolution of rose diagram in the development of CPB at different curing times: (a) 3d (b) 7d(c) 14d (d) 28d

During the development of CPB, the particles rolled slowly and horizontally without a simple translation. As the development proceeded, the particles tended to rotate from 80-100° and 260-280°, as shown in Fig. 16. The number of particles in the pre-developmental azimuth at different angles was not highly different. This was because the CPB particles were affected by the self-weight pressure. Although the directional arrangement was initially completed under the vertical pressure, the particle orientation distribution was still relatively uniform. The number of CPB particles changed in the azimuthal interval in the late developmental stage, the particles developed toward the middle gradually, and the final particle direction became stable in the middle.

3.6 Contact force chain of CPB

The force chain is in contact with the contact force by the self-weight pressure, and the

Accepted Manuscript Not Copyedited

contact force network form by the mutual connection created a force transmission chain (referred to as the force chain) [47]. The force chain is the path of the magnitude and direction of the force transmitted by the self-weight pressure through particle contact, which can intuitively reflect the local force of the PFC model. The thickness of the force chain represent the magnitude of the force, and the distribution of the force chain in an area can be regarded as the resultant force on particles. The change in the force chain also indicated the change in contact force between the particles and the contact deformation. During the development of CPB, the law of force chain development is shown in Fig. 16. The force chain was extremely sensitive to the self-weight pressure. Even in the same contact, a slight change in the self-weight pressure will cause the force chain to regenerate. As shown in Fig. 16, the force chain originated from the particles at the edge of the CPB, and the force chain diverged gradually and thickens to form a force chain network. When the curing time was 28d, the force chain network extended to all directions of the CPB, roughly along the diagonal, and then extended successively to finally reach the backfill area. At this time, the force chain reached the peak, the strong chain was the strongest, the weak force chain network was stable.

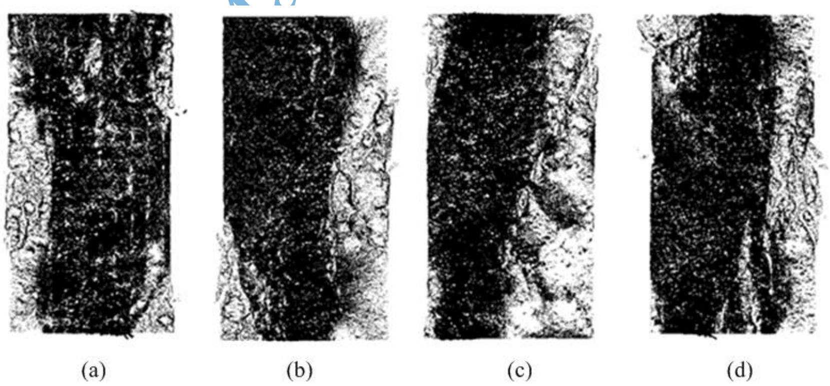

Fig. 16 Evolution of contact force chains in the development of CPB at different curing times: (a)3d (b)7d (c) 14d (d)28d

3.7 Contact force

CPB is a substance composed of many discrete particles, which contacts between adjacent particles form many force chains with different strengths, and their intersections form a

Accepted Manuscript Not Copyedited

network that does not run evenly through the backfill [48] .The strong chain and the weak chain are two important parts of the force chain network. Strong chains and weak chains act differently in resisting external loads. The strong chain is crucial in the external load, while the weak chain provides support for the strong chain and coordinates the overall deformation of the particle system.

3.7.1 Contact normal force

Fig. 17 shows the pole diagram of the contact normal force distribution corresponding to the CPB in the curing periods of 3, 7, 14, and 28d. The red line was the arithmetic mean of the contact force of the backfill particle system, and the solid line pole diagram was the result of numerical test statistics. As shown from Fig.17, the entire contact normal force rose diagram showed an “8” shape, and the whole sample exhibited anisotropy, which was consistent with the previous research regarding the contact normal direction. As the CPB developed, the normal contact force of the CPB increased. When the curing time was 28d, the strongest chain was reached, and the weak chain network was stable. That is to say, the CPB exhibited a stronger bearing capacity at this time, while the weak force chain provided support for the strong chain and coordinated the overall deformation of the particle system better, thus providing a strong support for the development of the contact force chain.

Accepted Manuscript Not Copyedited

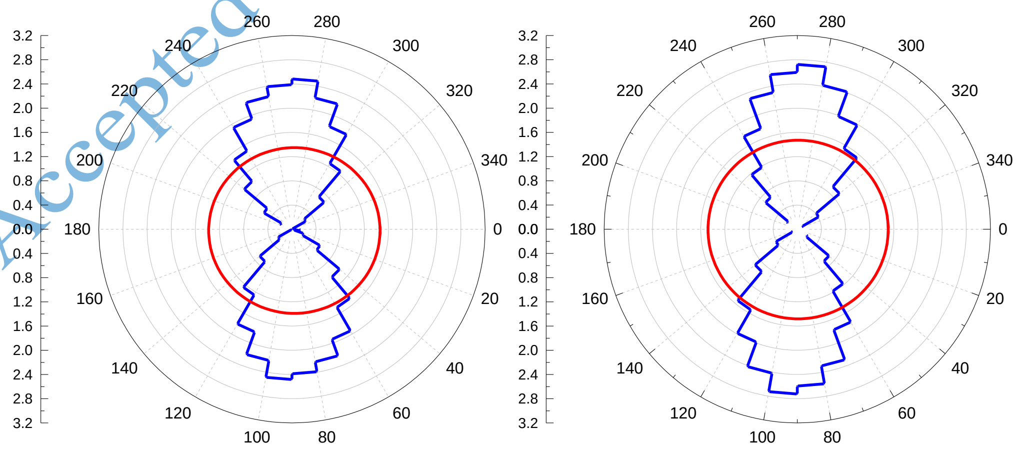

(a) (b)

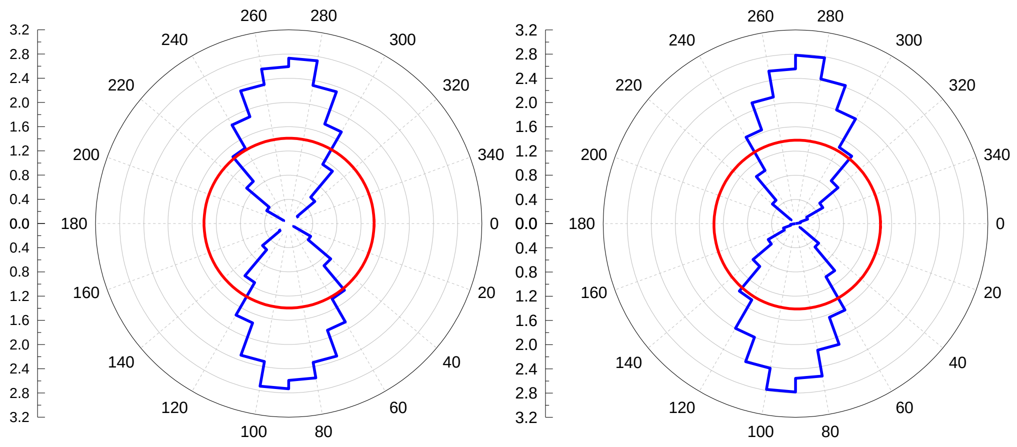

(c) (d)

Fig. 17 Distribution of contact normal forces at different curing times:

(a) 3d (b) 7d (c) 14d (d) 28d

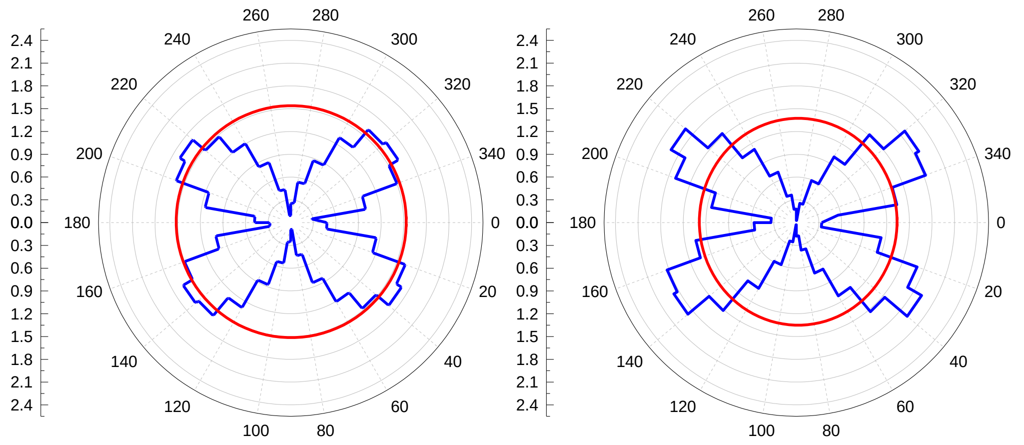

(a) (b)

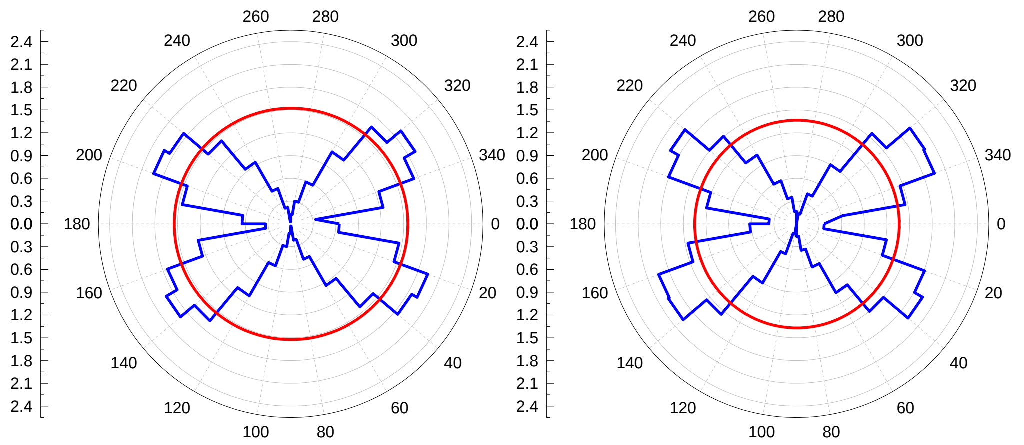

(c) (d)

Fig. 18 Distribution of contact tangential forces at different curing times:

(a) 3d (b) 7d(c) 14d (d) 28d

3.7.2 Contact tangential force

Fig. 18 shows the pole diagram of the contact tangential force distribution corresponding to the CPB in the curing periods of 3, 7, 14, and 28d . The red line was the arithmetic mean of the contact tangential force of the backfill particle system, and the solid line pole diagram was the result of numerical test statistics. As shown in Fig. 18, the entire contact tangential force rose diagram showed a "petal" shape, and the whole sample exhibited anisotropy, which was consistent with the previous research on contact normal direction and contact normal force [49]. As the CPB developed, the contact tangential force of the CPB increased. When the curing time was 28d, the maximum value of the tangential contact force of the CPB particles was reached. That is to say, the CPB exhibited a stronger bearing capacity at this time, while the weak force chain provided support for the strong chain and coordinated the overall deformation of the particle system in a better manner.

4 Conclusions

In this study, based on the SEM image of PFC modeling, the mesostructure characteristics of CPB at different curing times (3, 7 14 and 28 days) were studied and characterized. The relationship between the meso-structure and macro-mechanical properties of the CPB was discussed. The following conclusions are drawn：

a. Based on the powerful micromechanical property simulation software PFC2D for geotechnical materials, a PFC2D model of the mesostructure of CPB according to SEM images was proposed.

b. Based on the numerical simulation test of CPB, the detailed mesoscopic information, such as porosity, C_n, and contact force chain, which were difficult to obtain in laboratory tests, were obtained. For example, the coordination number of CPB decreased with the extension of curing time.

c. The numerical test of CPB based on PFC2D indicated that during the development of CPB, the particles rolled slowly and horizontally without a simple translation. The particles were not simply translational.

d. According to the PFC model established by SEM, the mesoscopic fabric of CPB was studied.

In the future, industrial CT imaging can be used to build a 3D PFC model, so as to have a deeper understanding of the internal structure of CPB. In addition, the PFC model based on SEM will promote the wider application of this technology in the analysis of other engineering materials (concrete, geotechnical, rock-soil mixture).

Conflicts of Interest

The authors declare that there are no conflicts of interest regarding the publication of this paper.

Acknowledgments

This research was supported by the National Natural Science Foundation of China (No. 51504182, 51674188, 51404191, 51405381), the Natural Science Basic Research Plan of Shaanxi Province of China (No. 2015JQ5187, 2018JQ5183, 2018JM5161), the Scientific Research Program funded by the Shaanxi Provincial Education Department (No. 15JK1466), the Project funded by China Postdoctoral Science Foundation (No. 2015M582685), and Outstanding Youth Science Fund of Xi'an University of Science and Technology (No. 2018YQ2-01). This research was also supported by the National Research Council of Science & Technology (NST) grant by the Korea government (MSIP) (No. CRC-16- 38502-KICT).

Data Availability

All data used to support the findings of this study are included within this paper.

Reference

[1]A. T. Cross and H. Lambers, Young calcareous soil chronosequences as a model for ecological restoration on alkaline mine tailings, *Sci. Total Environ.*, 607-608(2017), No.1, p. 608.

[2]L. Liu, Z. Fang, C. Qi, B. Zhang, L. Guo and K.-I. Song, Experimental investigation on the relationship between pore characteristics and unconfined compressive strength of cemented paste backfill, *Constr. Build. Mater.*, 179(2018) , p. 254.

[3]C. Qi, Q. Chen, A. Fourie and Q. Zhang, An intelligent modelling framework for mechanical properties of cemented paste backfill, *Miner. Eng.*, 123(2018), p. 16.

[4]C. Qi, Q. Chen, A. Fourie, J. Zhao and Q. Zhang, Pressure drop in pipe flow of cemented paste backfill: Experimental and modeling study, *Powder Technol.*, 333(2018), p. 9.

[5]A. Wu, Y. Wang, H. Wang, S. Yin and X. Miao, Coupled effects of cement type and water quality on the properties of cemented paste backfill, *Int. J. Miner. Process.*, 143(2015), p. 65.

[6]M. Fall and M. Pokharel, Coupled effects of sulphate and temperature on the strength development of cemented tailings backfills: Portland cement-paste backfill, *Cem. Concr. Compos.*, 32(2010), No.10, p. 819.

[7]H. Rong, Z. Min and H. Haobo, Pore structure evolution and its effect on strength development of sulfate-containing cemented paste backfill, *Minerals*, 7(2017), No.1, p. 8.

[8]Y. Wang, D. Liu and Y. Hu, Monitoring of internal failure evolution in cemented paste backfill under uniaxial deformation using in-situ X-ray computed tomography, *Arabian J. Geosci.*, 12(2019), No.5, p. 138.

[9]Q. Liu, D. Liu, Y. Tian and X. Liu, Numerical simulation of stress-strain behaviour of cemented paste backfill in triaxial compression, *Eng. Geol.*, 231(2017), p. 165.

[10]W. Xu and P. Cao, Fracture behaviour of cemented tailing backfill with pre-existing crack and thermal treatment under three-point bending loading: Experimental studies and particle flow code simulation, *Eng. Fract. Mech.*, 195(2018), p.129.

[11]S. Cao, E. Yilmaz and W. Song, Dynamic response of cement-tailings matrix composites under SHPB compression load, *Constr. Build. Mater.*, 186(2018), p. 892.

[12]E. Yilmaz, T. Belem and M. Benzaazoua, Study of physico-chemical and mechanical characteristics of consolidated and unconsolidated cemented paste backfills, *Gospodarka Surowcami Mineralnymi/mineral Resources Management*, 29(2013), No.1, p. 81.

[13]C. Qi and A. Fourie, Cemented paste backfill for mineral tailings management: Review and future perspectives, *Miner. Eng.*, 144(2019), art. 106025.

[14]Q. Chen, Q. Zhang, A. Fourie, X. Chen and C. Qi, Experimental investigation on the strength characteristics of cement paste backfill in a similar stope model and its mechanism, *Constr. Build. Mater.*, 154(2017), p. 34.

[15]Q. Chen, Q. Zhang, C. Qi, A. Fourie and C. Xiao, Recycling phosphogypsum and construction demolition waste for cemented paste backfill and its environmental impact, *J. Cleaner Prod.*, 186(2018), p. 418.

[16]M. Fall, M. Benzaazoua and S. Ouellet, Experimental characterization of the influence of tailings fineness and density on the quality of cemented paste backfill, *Miner. Eng.*, 18(2005), No.1, p. 41.

[17]L. Liu, Z. Y. Fang, Y. P. Wu, X. P. Lai, P. Wang and K.-I. Song, Experimental investigation of solid-liquid two-phase flow in cemented rock-tailings backfill using Electrical Resistance Tomography, *Constr. Build. Mater.*, 175(2018), p. 267.

[18]L. Liu, K.-I. Song, D. Lao and T.-H. Kwon, Rheological Properties of Cemented Tailing Backfill and the Construction of a Prediction Model, *Materials*, 8(2015), No.5, p.2076.

[19]D. Ouattara, T. Belem, M. Mbonimpa and A. Yahia, Effect of superplasticizers on the consistency and unconfined compressive strength of cemented paste backfills, *Constr. Build. Mater.*, 181(2018), p. 59.

[20]S. Cao, E. Yilmaz, W. Song, E. Yilmaz and G. Xue, Loading rate effect on uniaxial compressive strength behavior and acoustic emission properties of cemented tailings backfill, *Constr. Build. Mater.*, 213(2019), p. 313.

[21]H. Jiang, Z. Qi, E. Yilmaz, J. Han, J. Qiu and C. Dong, Effectiveness of alkali-activated slag as alternative binder on

workability and early age compressive strength of cemented paste backfills, *Constr. Build. Mater.*, 218(2019), p. 689.

[22]T. Yılmaz, B. Ercikdi and H. Deveci, Utilisation of construction and demolition waste as cemented paste backfill material for underground mine openings, *J. Environ. Manage.*, 222(2018), p. 250.

[23]Y. Huang, J. Li, Y. Teng, X. Dong, X. Wang, G. Kong and T. Song, Numerical simulation study on macroscopic mechanical behaviors and micro-motion characteristics of gangues under triaxial compression, *Powder Technol.*, 320(2017), p. 668.

[24]K. A. Yilmaz E, Ercikdi B., The factors affecting the strength and stability of paste backfill., *Yerbilimleri. Turk .Earth Sci.*, 28(2)(2003), No.28, p. 155.

[25]S. Cao, E. Yilmaz and W. Song, Fiber type effect on strength, toughness and microstructure of early age cemented tailings backfill, *Constr. Build. Mater.*, 223(2019), p. 44.

[26]L. Kong, F. X. Chen, L. I. Jie, S. O. Science and Q. T. University, Meso-direct-shear test of sand based on digital image correlation method and its PFC numerical simulation, *Rock Soil Mech.*, 34(2013), No.10, p. 2971.

[27]L. Liu, C. Zhu, C. Qi, B. Zhang and K.-I. Song, A microstructural hydration model for cemented paste backfill considering internal sulfate attacks, *Constr. Build. Mater.*, 211(2019), p. 99.

[28]Z. Song, H. Konietzky and M. Herbst, Three-dimensional particle model based numerical simulation on multi-level compressive cyclic loading of concrete, *Constr. Build. Mater.*, 225(2019), p. 661.

[29]G. Xue, E. Yilmaz, W. Song and S. Cao, Compressive strength characteristics of cemented tailings backfill with alkali-activated slag, *Appl. Sci.*, 8(2018), art. 6742392.

[30]X. Chen, X. Shi, J. Zhou, X. Du, Q. Chen and X. Qiu, Effect of overflow tailings properties on cemented paste backfill, *J. Environ. Manage.*, 235(2019) , p. 133.

[31]B. Zhang, J. Xin, L. Liu, L. Guo and K.-I. Song, An Experimental Study on the Microstructures of Cemented Paste Backfill during Its Developing Process, *Adv. Civ. Eng.*, 2018(2018) , p. 1.

[32]X. Qin, P. Wang, L. Liu, M. Wang and J. Xin, Sensitivity analysis of microstructure parameters and mechanical strength during consolidation of cemented paste backfill, *Math. Prob. Eng.*, 2018(2018) , p. 1.

[33]GB175-2007, Common Portland cement, (2007).

[34]L. Liu, J. Xin, C. Huan, C. Qi, W. Zhou and K.-I. Song, Pore and strength characteristics of cemented paste backfill using sulphide tailings: Effect of sulphur content, *Constr. Build. Mater.*, 237(2020), art. 117452.

[35]L. Liu, J. Xin, Y. Feng, B. Zhang and K.-I. Song, Effect of the cement–tailing ratio on the hydration products and microstructure characteristics of cemented paste backfill, *Arab. J. Sci. Eng.*, 44(2019), No.7, p. 6547.

[36]B. Sun, X. Wang and Z. Li, Meso-scale image-based modeling of reinforced concrete and adaptive multi-scale analyses on damage evolution in concrete structures, *Comput. Mater. Sci.*, 110(2015), p. 39.

[37]Y. Ju, H. Sun, M. Xing, X. Wang and J. Zheng, Numerical analysis of the failure process of soil–rock mixtures through computed tomography and PFC3D models, *Int. J. Coal Sci. Tech.*, 5(2018), No.2, p. 1.

[38]C. Liu, B. Shi, J. Zhou and C. Tang, Quantification and characterization of microporosity by image processing, geometric measurement and statistical methods: Application on SEM images of clay materials, *Appl. Clay Sci.*,54(2011), No.1, p. 97.

[39]W. Sun, K. Hou, Z. Yang and Y. Wen, X-ray CT three-dimensional reconstruction and discrete element analysis of the cement paste backfill pore structure under uniaxial compression, *Constr. Build. Mater.*, 138(2017), p. 1.69

[40]B. Koohestani, A. Khodadadi Darban and P. Mokhtari, A comparison between the influence of superplasticizer and organosilanes on different properties of cemented paste backfill, *Constr. Build. Mater.*, 173(2018), p. 180.

[41]J. Wu, M. H. El Naggar, X. Li and H. Wen, DEM analysis of geobag wall system filled with recycled concrete aggregate, *Constr. Build. Mater.*, 238(2020), art. 117684.

[42]C. Fan, *The direct shear test on clay materials based on particle flow code* [Dissertation], Chang'an University, 2017.

[43]X. Qin, L. Lang, W. Pai, W. Mei and X. Jie, Microscopic Parameter Extraction and Corresponding Strength Prediction of Cemented Paste Backfill at Different Curing Times, *Adv. Civ. Eng.*, 2018(2018), No.4, p. 1.

[44]M. C. Chen, K. Wang and L. Xie, Deterioration mechanism of cementitious materials under acid rain attack, *Eng. Fract. Mech.*, 27(2013), No.1, p. 272.
[45]N. P. Kruyt and L. Rothenburg, A strain–displacement–fabric relationship for granular materials, *Int. J. Solids Struct.*, 165(2019 , p. 14.
[46]J. H. Liu, Y. Wang, F. U. Kang-Lin and K. Zhong, Force analysis of anchor bolts reinforcing rock slope under simple harmonic vibration load, *Rock Soil Mech.*(2012), p. 85.
[47]J. Tian and E. Liu, Influences of particle shape on evolutions of force-chain and micro-macro parameters at critical state for granular materials, *Powder Technol.*,354(2019), p. 906.
[48]S. Chen, Z. Du, Z. Zhang, H. Zhang, Z. Xia and F. Feng, Effects of chloride on the early mechanical properties and microstructure of gangue-cemented paste backfill, *Constr. Build. Mater.*, 235(2020), art. 117504.
[49]Y. Liu, S. Wu and J. Zhou, Numerical simulation of sand deformation under monotonic loading and mesomechanical analysis, *Rock Soil Mech.*, 29(2008), No.12, p. 3199.